City Research Online

City, University of London Institutional Repository

Permanent repository link: https://openaccess.city.ac.uk/id/eprint/15669/

Link to published version: https://doi.org/10.1016/j.medengphy.2016.05.016

1   **Title page**

2

3

4   **Derivation of flow related risk indices for stenosed left anterior descending**

5   **coronary arteries with the use of computer simulations**.

6

7

8   Konstantinos P. Papadopoulos, Manolis Gavaises, Ioannis Pantos,

9   Demosthenes G. Katritsis and Nicholas Mitroglou.

10

11

12   Corresponding author: Konstantinos P. Papadopoulos

13   Email: Konstantinos.Papadopoulos.1@city.ac.uk, costis.papa@gmail.com

14   Telephone: +44 (0) 7580564404

15

1. Abstract

The geometry of the coronary vessel network is believed to play a decisive role to the initiation, progression and outcome of coronary artery disease (CAD) and the occurrence of acute coronary syndromes (ACS). It also determines the flow field in the coronary artery which can be linked to CAD evolution.

In this work geometric 3D models of left anterior descending (LAD) coronary arteries associated with either myocardial infarction (MI) or stable (STA) CAD were constructed. Transient numerical simulations of the flow for each model showed that specific flow patterns develop in different extent in the different groups examined. Recirculation zones, present distal the stenosis in all models, had larger extent and duration in MI cases. For mild stenosis (up to 50%) areas with low time averaged wall shear stress TAWSS (< 0.15Pa) as well as areas with high TAWSS (>3Pa) appeared only in MI models; in moderate and severe stenosis (>50%) these areas were present in all models but were significantly larger for MI than STA models. These differentiations were expressed via numerical indices based on TAWSS, oscillating shear index (OSI) and relative residence time (RRT). Additionally we introduced the coagulation activation index (CAI), based on the threshold behaviour of coagulation initiation, which exceeded the suggested threshold only for MI models with intermediate stenosis (up to 50%). These results show that numerical simulations of flow can produce arithmetic indices linked with the risk of CAD complications.

2. Introduction

The term coronary artery disease (CAD) describes the formation of atherosclerotic plaques in epicardial coronary arteries. The formed plaques cause the narrowing of

40   the vessel and reduce the blood and oxygen supply to the myocardium. In a

41   significant number of cases CAD leads to complications such as myocardial

42   infarction. These complications are often lethal and make CAD the leading cause or

43   mortality worldwide [1]. Patients diagnosed with CAD receive either pharmacological

44   treatment or coronary revascularization. The choice is based on the severity of the

45   stenosis and the clinical condition of the patient. However several patients receiving

46   pharmacological treatment suffer from complications while at the same time it is

47   possible that other patients take the risk of an unnecessary intervention [2].

48   While the triggering of thrombus formation is generally considered the rupture of an

49   atherosclerotic plaque, intracoronary ultrasound studies have suggested that plaque

50   rupture itself may not necessarily lead to clinical events [3-5]. Plaque ruptures have

51   been identified in patients with acute coronary syndromes at multiple sites away from

52   the culprit lesion (ACS) [3] and in patients with stable angina or asymptomatic

53   ischemia [4]. Therefore, plaque rupture seems to be a frequent event that requires

54   the contribution of additional factors in order to lead to ACS.

55   The idea of using quantitative characterization of the coronary geometry and flow

56   conditions as a dynamic risk factor for coronary disease is not novel [6, 7]. Several

57   studies on the distribution of atherosclerotic plaques in human arterial systems have

58   shown that atherosclerosis occurs predominantly at certain locations of the vascular

59   tree where the arteries have complex geometry that results in "disturbed" blood flow

60   behaviour [8-11]. Geometry [12] and flow [13] might also be responsible for the

61   thickening of the vessel wall a fact that is considered to predispose to atherogenesis

62   [14]. Statistical correlation lesion and the incidence of ACS [15] has also been

63   reported. Flow conditions influence the formation of thrombus via identified

3

64 mechanisms that act both on the vessel wall and on the biochemical reactions in

65 flowing blood. Mechanical stimulation can influence the endothelium cells' response

66 [16, 17]; wall shear stress (WSS) can also affect the vulnerability [18], the evolution

67 [19] and even the composition of plaques [20] while mechanical stresses contribute

68 to the rupture of the plaques. Flow directly influences the reactions related to

69 thrombus formation by regulating the transport of involved substances [21];

70 pathological shear distribution can independently activate the coagulation

71 mechanism [22]; platelet deposition is correlated to flow patterns like flow separation,

72 and recirculation [23, 24]. These findings indicate that the thrombogenic potential of

73 a partially blocked coronary artery can be linked to characteristics of the flow field.

74 As coronary network is located on the heart, it follows the contractions of the heart

75 muscle. This has been simulated [25-27] .and it has been shown to influence the

76 flow distribution in the bifurcations [27] while it has no significant effect on

77 (computed) time averaged values of WSS [25, 27, 28]. The rheological behaviour of

78 blood is also complex, as it exhibits shear thinning behaviour for low values of shear

79 rate. However, for coronary flow conditions this is important for lower values of inlet

80 flow rate [29] occurring during a small part of the cardiac cycle [25, 30]. So, in most

81 related studies it is modelled as a Newtonian fluid [26, 31-36]. For the flow rate in the

82 coronary inlet a number of different approaches have been proposed. 'Average' and

83 widely accepted waveforms for the mass flow and the inlet pressure that can be

84 found in literature [25, 26], obtained from MRI [37] or catheter [38] measurements or

85 animal models [33, 34, 39], in vitro measurements [26, 40]. Simplified pulses with

86 adjusted average mass flow rate have also been used [27, 38], as it has been

87 demonstrated that the exact form of the inlet pulse has small influence over the time

88   averaged quantities [38]. The problem of the outlet boundary conditions is more

89   complicated, as the outflow of the main branches of the coronary is mainly

90   determined by the unknown downstream vessel network. In the case of healthy

91   vessel the flow rate in each branch can be defined under the assumption of (almost)

92   constant WSS and Poiseuille flow [25, 31]. A more sophisticated approach for the

93   boundary conditions is the use of lumped parameter models analogous to electrical

94   circuits for the inlet/ outlet of the computational domain. These models impose

95   relationships between the pressure and the mass flow and in some cases their time

96   integrals and derivatives at each boundary [41-44].

97   Existing computational studies on coronary flow have been proved in good

98   agreement with in-vitro experimental results [40]. A number of the published works

99   focus on the effect of different parameters on the results, such as the motion of the

100   vessels [25-27], the existence of bifurcations [45], the off-plane geometry of the

101   coronary and the small alterations of the geometry [40] and the use of non-

102   Newtonian models for blood viscosity [25, 29, 30]. Other studies apply computational

103   techniques on several problems related to coronary flow that cannot be accessed by

104   experiments or medical examinations, as the study of flow patterns for different types

105   of atheromatic plaques [36], the comparison of different cases of coronary

106   anastomosis [46], pre and post stenting haemodynamics [31, 33, 47], the effect of

107   foreshortening (deformation) of stents on WSS [34], different methods and types of

108   coronary aneurysm stenting [48] recently CFD of blood flow has been used as

109   diagnostic method of stenosis-caused ischemia, via the calculation of the fractional

110   flow reserve [49, 50].

111 We have previously shown that a combination of specific anatomic parameters

112 predispose to vulnerable plaque development, rupture of the plaque and consequent

113 thrombosis [51, 52]. In the present study we hypothesized that the different risk for

114 ACS that was statistically attributed to different LAD models can be quantified via

115 specific flow related quantities. These quantities are calculated from the flow field as

116 it is obtained with the use of computational fluid dynamics (CFD) simulations. Finally,

117 using the CFD results we established a set of risk indices appropriate for

118 assessment of an arbitrary case.

119 **3. Materials and methods**

120 *Coronary models*

121 Geometric models of coronary arteries were obtained from previous analyses of

122 patients with an anterior ST-elevation myocardial infarction (MI) and a patent LAD or

123 patients with stable coronary stenoses (STA) and a significant LAD stenosis via

124 coronary angiography [52]. Statistical analysis indicated that coronary stenoses

125 associated with MI were closer to the ostium (inlet) of the LAD compared with

126 stenoses associated with stable CAD. Additionally, in patients with stable CAD the

127 stenosed part of the vessel does not involve bifurcations whereas in MI models there

128 are bifurcations within the stenotic lesion. In our study we used two different groups

129 associated with ACS, MI1 and MI2, according to the statistical analysis [52, 53]. The

130 difference between the MI1 and MI2 models is the location of the affected side-

131 branch: in MI1 models it is located upstream the peak of the stenosis while in MI2

132 models it is located downstream the peak of the stenosis.

133　Based on these characteristics an 'average' healthy LAD model [52] was

134　constructed, consisting of one main branch and 5 side branches (6 outflows), with

135　total volume $6.922 \cdot 10^{-7} m^3$ and total wall surface $0.0012 \ m^2$.

136　Starting from the healthy LAD geometry the models with maximum stenosis (90%)

137　associated either with MI (MI1 and MI2) or with stable CAD (STA) were constructed

138　(Figure 1)., by introducing a sinusoidal radius reduction as done in previous studies

139　[34, 35, 54-56]. The geometries with intermediate degrees of stenosis were obtained

140　via linear interpolation.

141　As mesh independence tests indicated that above 1 million cells the results did not

142　change significantly (~2%) for outlet pressures and WSS, computational grids of

143　about 1.5 million hexahedral cells were created for each geometry, using the Hexa-

144　Block tool of ANSA [57]. 16 different geometries were used for the simulations

145　(Figure 1), one healthy and 15 with different degrees of stenosis The results for the

146　models with 90% of stenosis were used only to investigate the flow-rates calculated

147　from the boundary conditions.

148　*Fluid model and boundary flow conditions*

149　Blood was modelled as a Newtonian fluid with the use of the incompressible Navier-

150　Stokes equations, as for LAD dimensions the shear rate is well above the limit where

151　blood exhibits shear –thinning behaviour for almost the whole of the cardiac cycle

152　[25, 30, 58]. Flow was modelled as laminar (no turbulence model used) as the

153　calculated Reynolds numbers were below 100 even for 90% stenosis. The vessel

154　walls were considered rigid and stationary and no slip boundary condition was

155　imposed for the walls.

156   Except from the resistance of the coronary arterial network, the movement of the

157   heart muscle is the main determining factor, as the vessels that enter the

158   myocardium are compressed due to contractions. As the structure of the coronary

159   network for each case is inaccessible, the boundary conditions always include some

160   assumptions, and the results are approximate. In this study the method of boundary

161   conditions is based on three main hypotheses: (i) the existence of the stenosis is not

162   changing the aortic pressure or the behaviour of the coronary network downstream

163   the computational domain; (ii) the behaviour of the downstream network can be

164   approximated by a time depended resistance; (iii) WSS(τ_w) for the computational

165   domain of the healthy case is almost constant and approximately 1.5 Pa [8] and flow

166   is approximately Poiseuille [2, 6, 7].

167   For the healthy coronary model inlet, a generic waveform for the coronary mass flow

168   [5-7] was used; the resulting average velocity at the inlet is shown in Figure 2. Under

169   the assumption of constant WSS, the distribution of flow rate among the main

170   branch Q_m and the i-th side branch $Q_{i,0}$ is determined by the radii ($r_{m,i}$, r_i) of the two

171   branches, and it follows Equation 1 (μ is the fluid viscosity):

172     $$\tau_w = \frac{4\mu Q}{\pi r^3} \Longrightarrow \cdots \Longrightarrow \frac{Q_{i,0}}{r_i^3} = \frac{Q_{m,i}}{r_{m,i}^3}$$

173   *Equation 1*

174   From Equation 1, the flow rate fraction for the LAD branch (0.52, based on the

175   diameters of the vessels) and the flow rates for each branch of the computational

176   domain can then be expressed as a function of the radii of the main and the side

177   branches at the sites of bifurcations (Equation 2):

8

178 $$Q_i = Q_{tot} \cdot f(r_1, \ldots, r_i) = Q_{tot} \cdot f_i$$

179 *Equation 2*

180 $$f_i = (1 - \sum_{n=1}^{i-1} f_n) \cdot \frac{r_i^3}{r_i^3 + r_{m,i}^3}$$

181 Simulation obtained for the non-stenosed (healthy) model showed small variation of

182 WSS, with more than 99% of the vessel wall surface having TAWSS values in the

183 range 1-3Pa; these values are within the reported non-pathological arterial range [8].

184 From the simulations for the healthy model the pressure drop between the inlet and

185 each outlet i ($\Delta P_{out,i}$) of the computational domain were obtained. The aortic pressure

186 pulse [9], (Figure 2), and atrial pressure were used as inlet and far out pressure. The

187 the calculated pressure drops ($\Delta P_{out,i}$), mass flow rates ($Q_{out,i}$) for each outlet of the

188 healthy model are linked with the time dependent resistance (R_i) downstream each

189 outflow with the relation:

190 $$\Delta P_{tot}(t) = \Delta P_{out,i}(t) + Q_{out,i}(t) \cdot R_i(t)$$

191 *Equation 3*

192 Using Equation 3 and the values of flowrates and pressure drops from the simulation

193 of the healthy model, the downstream resistance $R_i(t)$ for each outflow was

194 calculated.

195 For the stenosed models, the pressure pulse of Figure 2was used as inlet boundary

196 c

197 o

304 *Equation* 3 and the values of the downstream resistance calculated from the non-

198 n

305 stenosed model. The boundary condition applied at the outlets was 'target mass

199 d

306 flow' as described in the Ansys Fluent User's Guide [1] combined with a User

200 i

9

201 t

202 i

203 o

307   Defined Function (UDF); the applied algorithm used for the calculation of the flow

308   rate at each outlet is shown in Figure 3. The mass flow at the inlet Q_{in} was calculated

309   from **Error! Reference source not found.** to satisfy the mass conservation.

310
$$Q_{in} = \sum_i Q_{out,i}$$

311   *Equation 4*

312   In order to avoid stability issues a very small under-relaxation factor (0.05) was used

313   for the pressure correction, combined with a sufficient number of iterations (~200) for

314   each timestep in order to ensure stabilization of the mass flow rate values at the

315   outlets before moving on to the next timestep. A number of cardiac cycles (3-4) was

316   simulated for each case in order to eliminate any effect of the initial flow field; as the

317   calculated flow rates were identical after the 2nd cardiac cycle, only the results of the

318   last cycle have been processed. To verify the above process, we applied outflow

319   resistance boundary conditions on the healthy vessel and the results were almost

320   identical (less than 1% variation) with the results obtained with the assumption of

321   constant WSS.

322   Finally, further analysis of the results obtained with the above method, indicated a

323   simplified approximation for estimating the resistance downstream each branch. For

324   the non-stenosed model the pressure drop between the inlet and the outlets ($\Delta P_{out,i}$)

325   was found to be very small (<4%) compared to the total pressure drop. Thus, the

326   downstream resistance could be estimated using Equation 5:

327
$$R_i = \frac{\Delta P_{tot} - \Delta P_{out,i}}{Q_{tot} \cdot f_i} \approx \frac{\Delta P_{tot}}{Q_{tot} \cdot f_i} = \frac{R_{tot}}{f_i}$$

328   *Equation 5*

329   This approximation results to a small (less than 2%) increase of the calculated flow

330   rates, but it allows for the method to be applied on any arbitrary stenosed geometry

331   without necessitating simulations for non-stenosed model as the values for the

332   downstream resistance can be derived directly from Equation 3 and Equation 5,

333   avoiding the simulations for the non stenosed model.

334

335

336   As a test, we applied outflow resistance boundary condition on the healthy vessel

337   and the results were almost identical (less than 1% variation) with the results

338   obtained with the assumption of constant WSS.

339   All flow simulations were performed in Fluent. The The time averaged WSS vector

340   and magnitude (TAWSS and TAWSS$^{(V)}$),oscillating shear index (OSI) and relative

341   residence time (RRT) were computed according to the following formulas [48, 62]

342   using the META [57] post processor:

343
$$TAWSS = \frac{1}{T} \int_0^T |\overrightarrow{WSS}| dt,$$

344   *Equation 6*

345
$$TAWSS^{(V)} = \frac{1}{T} \left| \int_0^T \overrightarrow{WSS} dt \right|$$

346   *Equation 7*

347
$$OSI = 0.5 \times \left(1 - \frac{\left| \int_0^T \overrightarrow{WSS} dt \right|}{\int_0^T |\overrightarrow{WSS}| dt} \right)$$

348   *Equation 8*

349
$$RRT = [(1 - 2 \times OSI) \times TAWSS]^{-1}$$

350   *Equation 9*

11

351   In brief, OSI expresses the variation in the direction of the WSS (and velocity) vector

352   in respect to the dominant direction of the flow, while RRT gives a relative estimation

353   of the residence time of the fluid in an area, as it has increased values in the areas

354   where the near-wall velocity has large direction changes over one period and small

355   magnitude.

356   *Coagulation activation index (CAI)*

357   The activation of the coagulation process occurs within an area of the vessel wall

358   where a triggering stimuli exists, either due to rapture of atheromatous plaque or

359   possibly due to alteration of the behaviour of endothelium cells caused by

360   pathological flow conditions. However the stimulation does not guarantee the

361   activation of the coagulation process. It has been demonstrated [63] that the initiation

362   of the coagulation exhibits a threshold behaviour with respect to wall shear rate and

363   the stream-wise length of the triggering surface. A feasible explanation for this

364   behaviour is that a minimum contact time between the blood flowing reactants and

365   the reacting surface is required for the transition from the initiation to the

366   amplification phase of coagulation. In order to estimate this flow-related aspect of the

367   coagulation process in this study we introduce the coagulation activation index (CAI)

368   as follows.

369   The initiation reactions occur in a small layer of depth h above the reacting area.

370   Considering steady flow conditions, the value of wall shear rate γ determines the

371   flow velocity at a specific distance h near the wall, $u = \gamma \cdot h$. If the reacting area has

372   a constant stream-wise length L the contact time between the flowing substances

373   and the reacting surface is approximately:

$$t_{res} = \frac{L}{u} = \frac{2L}{\gamma h}$$

374

375

376   Under the reasonable approximation that the reaction zone depth does not change

377   significantly for different values of shear, a threshold value for the quantity L/γ can

378   be defined regarding the activation of the coagulation process. From the threshold

379   conditions for the initiation of the coagulation process previously reported in respect

380   to the wall shear rate and the stream-wise length of the reacting area [63] the

381   threshold value for CAI was calculated $0.8 - 1 \times 10^{-5} m \times s$.

382   In order to estimate this in our results we used the CAI, defined as $\sqrt{S}/\gamma_{th}$ where S is

383   the area where the average wall shear rate was below a certain value, in this study

384   we used $\gamma < 43\ s^{-1}$-. As threshold value for CAI we used $1.2 \times 10^{-5} m \times s$,

385   approximately 10% above the value calculated for the non stenosed case and close

386   to the value calculated with the use of the experimental data [63].

387   **4. Results**

388   *Flow rates*

389   In all coronary models with induced stenosis, mass flow rate is reduced compared to

390   the healthy case at the inlet and at the outlet of the side branches distal to the peak

391   of the stenosis similar to previous works [47, 60]. However as shown in Table 1 only

392   high degrees of stenosis ($\geq 70\%$) have significant impact on the mass flow rate at

393   the inlet and the outlets distal the stenosis while the flow rate in the branches

394   upstream the stenosis exhibit small (.<4%) variation.

395   *Flow recirculation*

13

396   Recirculation zones were observed distal to the lesion for some part of the cardiac

397   cycle in all models with stenosis of 50% and above and for the MI1 model with 35%.

398   In MI1 and MI2 models these zones were larger, and occupied a larger fraction of

399   the cycle. It is also interesting that in the cases MI1 mainly but also in MI2 part of the

400   recirculating flow ends up in the side branch (magenta streamlines in Figure 4), and

401   in some cases there is also a small recirculation zone in the side branch distal the

402   stenosis, something that was not observed in STA models. The velocity profiles of

403   the normal (0% stenosis) and the diseased models downstream the stenosis differ

404   considerably (Figure 5). In the cases of 70% stenosis a jet-like flow develops in the

405   vessel whereas in specific areas of the cross section the average velocity is opposite

406   to the main flow direction (Figure 5). Note that a small difference in the location of

407   the stenosis (<3mm, less than 20% of the total length of the whole lesion) as it is

408   between MI1 and MI2, changes significantly the location of the areas with inversed

409   average flow velocity.

410   *Flow parameters*

411   The surface averaged values for TAWSS (Table 2) and RRT and OSI (Table 3) for

412   the whole vessel surface had small variations among the considered models. The

413   area averaged TAWSS for the whole vessel wall was 0.7-1.1Pa for all models, within

414   the range measured in vivo [64]. Based on the results of the healthy model and also

415   on literature data (for TAWSS) [7, 32, 33, 45, 65] we calculated the areas with low

416   (<0.15Pa) and high TAWSS (>3Pa) (Table 1), high OSI (>0.3) and RRT (>15) (Table

417   3) for each model. Areas with high TAWSS are located at the stenotic lesion and are

418   larger for higher degrees of stenosis, while areas with low TAWSS, found

419 downstream the stenosis (Figure 6) are mainly present in cases with stenosis up to

420 50%. The size of these areas generally larger for MI models (Table 2).

421 RRT (Figure 7) and OSI had significant variations at the areas of the recirculation

422 zones shown in Figure 7. The differentiation of the values (especially this of RRT)

423 was in accordance to the bigger size and duration of the recirculation zones for MI

424 cases (Table 3). Finally, in order to demonstrate the difference of the distribution of

425 OSI and RRT among different groups we calculated the magnitude of surface where

426 OSI and RRT are above specific values. As shown in Figure 8 the extent of the

427 vessel wall with high OSI and RRT was significantly greater for the MI1 and MI2

428 models for the cases of moderate and high degrees of stenosis (>35%).

429 *Risk indices*

430 Using the calculated flow parameters we sought to propose a set of arithmetic risk

431 indices that describe the susceptibility to deterioration and coronary thrombosis. The

432 indices express the magnitude of the vessel wall where the calculated values have

433 extremely low (only for TAWSS) or high values. The thresholds proposed for the

434 indices are summarized in Table 4

435 As shown in Table 5 for intermediate stenosis (50%) in the MI1 and MI2 models all

436 indices exceed the threshold values while even for mild stenosis (20% and 35%)

437 some of the indices of the MI1 and MI2 models also exceeded the threshold values.

438 For the most severe stenosis (70%) all indices thresholds except Low TAWSS were

439 exceeded for all models.

440 The calculated CAI values for each model are shown in Figure 9 together with the

441 threshold value (dotted line). All considered stenosis for the MI2 model result in CAI

442 values above the threshold value whereas for the MI1 model the threshold is

443 exceeded only for the intermediate stenosis (35% and 50%). For the STA model the

444 threshold value is exceeded only in the case of the most severe stenosis (70%).

445 Nevertheless in STA and MI2 model with 70% stenosis the value of CAI is slightly

446 above the threshold therefore the result cannot lead to safe conclusion.

447

448 **5. Discussion**

449 We presented CFD results in a number of LAD models which are associated either

450 with MI or with stable CAD. The boundary conditions were based both on geometry

451 and aortic pressure and gave reasonable results in terms of flow rates (which mainly

452 determine the WSS values [29, 38, 66]) and can be applied on any coronary

453 geometry. The whole process has low computational cost and can be performed with

454 the use of commercial home computers. The simulations presented in this work were

455 performed using a single processor of an Intel i-7 330GHz computer. Each cardiac

456 cycle consisted of 200 time-steps, required approximately 16h CPU time and used

457 approximately 4GB of RAM.

458 The relationship of hemodynamic factors and thrombus formation has been

459 previously investigated in various experimental and CFD studies [23, 24, 67, 68]. In

460 these studies the flow parameters than have been most closely associated with

461 thrombosis are surface related, mainly WSS, as It is generally accepted that low

462 WSS promotes atherosclerosis and vulnerable plaque formation [69, 70] and

463 possibly alters the endothelium properties [16, 17]. Therefore low TAWSS values in

464 a large area of the vessel imply increased possibility for both deterioration and

465 thrombosis. These conditions were expressed via the index related to low TAWSS

16

466 value and the value of this index was significantly higher in MI1 and MI2 geometries

467 with 35% and 50% stenosis (Table 5)

468 High WSS may trigger plaque rupture but the evidence on that is weak [70, 71]. In

469 any case, at least for the examined models, the index related to high TAWSS

470 depends strongly on the degree of the stenosis while extremely high values of shear

471 stress (>30 Pa), capable of causing platelet activation [72] were observed only in the

472 cases of severe stenosis (>70%) and in a very small part of the vessel surface. In

473 respect to shear induced platelet activation and the effect of high values of WSS it is

474 possibly of more interest to examine the exposure time of platelets to high values of

475 shear stress or stress accumulation along the streamlines [23] than looking into local

476 values.

477 The increased residence time and the recirculation in the post stenotic region are

478 expressed via the RRT and OSI. The RRT index has clearly higher values (>3) in all

479 cases where recirculation occurs near the recirculation zone (Table 5 and Figure 5

480 and Figure 7). OSI related index has similar variation to RRT (Table 5) and at least

481 for the examined models does not provide any additional information. RRT and OSI

482 indices have distinctively higher values for the cases where recirculation zones were

483 observed and the variation of their values is in accordance to the different size and

484 duration of the vortices observed via visualization.

485 Previous studies also showed that slowly recirculating flow due to core jet flow

486 patterns through a stenosis promote aggregation of platelets and that blood

487 stagnation occurring at areas with disturbed flow may facilitate the accumulation of

488 blood thrombogenic factors near the wall [73]. Since adhesion of platelets to a

489 surface is greatly enhanced by prior stimulation [74], this mechanism offers an

17

490   explanation for the increased platelet deposition at the recirculation zone. An

491   estimation of the strength of this mechanism can be obtained using the the product

492   of the high TAWSS and the RRT related indices (Table 5). In cases with elevated

493   values of TAWSS (50% and 70%) stenosis, for STA models is around 40 while for MI

494   it is above 55.

495   Finally, the CAI index significantly exceeds the calculated threshold only in MI1 and

496   MI2 cases with intermediate (35-50%) stenosis (Figure 9) showing that in these

497   cases there are areas with higher probability of coagulation initiation. It is interesting

498   to note here that when we applied the thrombin submodel [75] on two cases

499   described in [63], the ratio of the CAI (0.8) matched exactly the ratio of the maximum

500   thrombin concentration (0.799) and was really close to the ratio of the average

501   thrombin generation downstream the reacting area (0.759)[76]. This could indicate

502   that CAI, while calculated via flow simulations is strongly related to the

503   thrombogenetic potential of pathological flow.

504   Regarding the examined cases it can be said that the calculated quantities generally

505   agree the statistically derived risk assumption, showing that the MI2 models are of

506   higher risk, followed by MI1 models while STA models appear by far less dangerous.

507   The visualization of the results correlated the indices with the calculated flow field

508   and pointed out the specific vessel segments where the local flow conditions (are

509   assumed to) predispose to thrombosis. These parts of the vessel surfaces were

510   within the areas of interest (near and downstream the stenotic lesion) and not in

511   random sites of the geometry. It is remarkable that CAI, while derived using data

512   from experiments performed in a different context was found in very good agreement

513   with the statistical hypothesis.

18

514   The proposed method is possibly overlapping with already published works for

515   coronary assessment based on anatomy [53] or on combined data related to

516   anatomy and WSS [45] but it attempts a more detailed assessment as it suggests 5

517   flow related indices. Additionally, as we believe that for biological processes the

518   actual size of the quantities is important, our results are normalized but they are not

519   non-dimensional. As flow simulations are not able to follow the variations of the flow

520   conditions due to changes to blood pressure and heart beat rate, this is still mainly a

521   geometrical assessment, but as it also shows (e.g. MI1 and MI2 models with 20% of

522   stenosis) that small geometry changes can result to significantly different values for

523   flow parameters.

524   The main weakness of this work is the relatively small number (13) of examined

525   cases and the non-variation of the general LAD shape, as all models were derived

526   from a single initial geometry, obtained by three-dimensional reconstruction of

527   conventional coronary angiography images [77]. However, as medical imaging

528   techniques advance, coronary models appropriate for CFD simulations can also be

529   derived with the use of non-invasive methods as computed tomography coronary

530   angiography [78, 79] or rotational angiography [49] thus making the future

531   application of the method easier. Obviously before such a tool is ready for use in

532   clinical practice it is necessary to apply the underlying methodology in large numbers

533   of real patients' coronary geometries with known outcome in order to validate and

534   possibly modify the range of non-pathological values of the indices suggested here.

535   Additionally, as the proposed indices are sensitive to small geometry changes, the

536   range of the non-pathological values should be related to the accuracy of the

537   imaging and reconstruction methods.

6. Conclusions

A method for coronary flow simulations was presented and applied on a set of geometrical models previously characterized as of low or high complication risk. The results revealed that culprit flow patterns are present to a greater extent in the geometries characterized as of high risk. Additionally, it was demonstrated that disturbed flow can be expressed via arithmetic quantities instead of just visualized via plots. The quantitative expression of pathological flow patterns can make possible the use of CFD simulation as an additional tool for estimating the complication risk in stenosed coronary vessels.

7. Acknowledgements

8. References

[1] Roger VL, Go AS, Lloyd-Jones DM, Adams RJ, Berry JD, Brown TM, et al. Heart disease and stroke statistics--2011 update: a report from the American Heart Association. Circulation. 2011;123:e18-e209.

[2] Patel MR, Dehmer GJ, Hirshfeld JW, Smith PK, Spertus JA. ACCF/SCAI/STS/AATS/AHA/ASNC 2009 Appropriateness Criteria for Coronary RevascularizationA Report by the American College of Cardiology Foundation Appropriateness Criteria Task Force, Society for Cardiovascular Angiography and Interventions, Society of Thoracic Surgeons, American Association for Thoracic Surgery, American Heart Association, and the American Society of Nuclear Cardiology Endorsed by the American Society of Echocardiography, the Heart Failure Society of America, and the Society of Cardiovascular Computed Tomography. J Am Coll Cardiol. 2009;53:530-53.

[3] Hong MK, Mintz GS, Lee CW, Kim YH, Lee SW, Song JM, et al. Comparison of coronary plaque rupture between stable angina and acute myocardial infarction: a three-vessel intravascular ultrasound study in 235 patients. Circulation. 2004;110:928-33.

[4] Maehara A, Mintz GS, Bui AB, Walter OR, Castagna MT, Canos D, et al. Morphologic and angiographic features of coronary plaque rupture detected by intravascular ultrasound. Journal of the American College of Cardiology. 2002;40:904-10.

569   [5] Rioufol G, Finet G, Ginon I, Andre-Fouet X, Rossi R, Vialle E, et al. Multiple atherosclerotic plaque
570   rupture in acute coronary syndrome: a three-vessel intravascular ultrasound study. Circulation.
571   2002;106:804-8.
572   [6] Zhu H, Ding Z, Piana RN, Gehrig TR, Friedman MH. Cataloguing the geometry of the human
573   coronary arteries: a potential tool for predicting risk of coronary artery disease. International Journal
574   of Cardiology. 2009;135:43-52.
575   [7] Wellnhofer E, Osman J, Kertzscher U, Affeld K, Fleck E, Goubergrits L. Non-dimensional modeling
576   in flow simulation studies of coronary arteries including side-branches: A novel diagnostic tool in
577   coronary artery disease. Atherosclerosis. 2011;216:277-82.
578   [8] Giddens DP, Zarins CK, Glagov S, Bharadvaj BK, Ku DN. Flow and atherogenesis in the human
579   carotid bifurcation. In: Schettler G, editor. Fluid Dynamics as a Localizing Factor for Atherosclerosis:
580   Spinger-Verlag Press; 1993.
581   [9] Kassab GS, Fung YC. The pattern of coronary arteriolar bifurcations and the uniform shear
582   hypothesis. Ann Biomed Eng. 1995;23:13-20.
583   [10] Ku DN, Giddens DP, Zarins CK, Glagov S. Pulsatile flow and atherosclerosis in the human carotid
584   bifurcation. Positive correlation between plaque location and low oscillating shear stress.
585   Arteriosclerosis, Thrombosis, and Vascular Biology. 1985;5:293-302.
586   [11] Asakura T, Karino T. Flow patterns and spatial distribution of atherosclerotic lesions in human
587   coronary arteries. Circulation Research. 1990;66:1045-66.
588   [12] Friedman MH, Baker PB, Ding Z, Kuban BD. Relationship between the geometry and quantitative
589   morphology of the left anterior descending coronary artery. Atherosclerosis. 1996;125:183-92.
590   [13] Irace C, Cortese C, Fiaschi E, Carallo C, Farinaro E, Gnasso A. Wall Shear Stress Is Associated With
591   Intima-Media Thickness and Carotid Atherosclerosis in Subjects at Low Coronary Heart Disease Risk.
592   Stroke. 2004;35:464-8.
593   [14] Stary H, Blankenhorn D, Chandler AB, Glagov S, Insull Jr W, Richardson M, et al. A definition of
594   the intima of human arteries and of its atherosclerosis-prone regions. A report from the Committee
595   on Vascular Lesions of the Council on Arteriosclerosis, American Heart Association. Circulation.
596   1992;85:391.
597   [15] Katritsis DG, Efstathopoulos EP, Pantos I, Tzanalaridou E, De Waha A, Siontis GCM, et al.
598   Ruptured versus stable plaques in human coronary arteries. Coronary Artery Disease. 2011;22:345-
599   51 10.1097/MCA.0b013e3283471f95.
600   [16] Malek AM, Alper SL, Izumo S. Hemodynamic shear stress and its role in atherosclerosis. JAMA:
601   the journal of the American Medical Association. 1999;282:2035-42.
602   [17] Davies PF, Tripathi SC. Mechanical stress mechanisms and the cell. An endothelial paradigm.
603   Circulation Research. 1993;72:239-45.
604   [18] Slager CJ, Wentzel JJ, Gijsen FJH, Schuurbiers JCH, van der Wal AC, van der Steen AFW, et al. The
605   role of shear stress in the generation of rupture-prone vulnerable plaques. Nat Clin Pract Cardiovasc
606   Med. 2005;2:401-7.
607   [19] Gibson CM, Diaz L, Kandarpa K, Sacks FM, Pasternak RC, Sandor T, et al. Relation of vessel wall
608   shear stress to atherosclerosis progression in human coronary arteries. Arteriosclerosis, Thrombosis,
609   and Vascular Biology. 1993;13:310-5.
610   [20] Samady H, Eshtehardi P, McDaniel MC, Suo J, Dhawan SS, Maynard C, et al. Coronary Artery
611   Wall Shear Stress Is Associated With Progression and Transformation of Atherosclerotic Plaque and
612   Arterial Remodeling in Patients With Coronary Artery Disease. Circulation. 2011;124:779-88.
613   [21] Hathcock JJ. Flow Effects on Coagulation and Thrombosis. Arteriosclerosis, Thrombosis, and
614   Vascular Biology. 2006;26:1729-37.
615   [22] Jackson SP, Nesbitt WS, Westein E. Dynamics of platelet thrombus formation. Journal of
616   thrombosis and haemostasis : JTH. 2009;7 Suppl 1:17-20.
617   [23] Bluestein D, Niu L, Schoephoerster RT, Dewanjee MK. Fluid mechanics of arterial stenosis:
618   relationship to the development of mural thrombus. Ann Biomed Eng. 1997;25:344-56.

619 [24] Raz S, Einav S, Alemu Y, Bluestein D. DPIV prediction of flow induced platelet activation-
620 comparison to numerical predictions. Ann Biomed Eng. 2007;35:493-504.
621 [25] Theodorakakos A, Gavaises M, Andriotis A, Zifan A, Liatsis P, Pantos I, et al. Simulation of cardiac
622 motion on non-Newtonian, pulsating flow development in the human left anterior descending
623 coronary artery. Physics in Medicine and Biology. 2008;53:4875.
624 [26] Prosi M, Perktold K, Ding Z, Friedman MH. Influence of curvature dynamics on pulsatile coronary
625 artery flow in a realistic bifurcation model. Journal of Biomechanics. 2004;37:1767-75.
626 [27] Pivkin IV, Richardson PD, Laidlaw DH, Karniadakis GE. Combined effects of pulsatile flow and
627 dynamic curvature on wall shear stress in a coronary artery bifurcation model. Journal of
628 Biomechanics. 2005;38:1283-90.
629 [28] Figueroa CA, Vignon-Clementel IE, Jansen KE, Hughes TJR, Taylor CA. A coupled momentum
630 method for modeling blood flow in three-dimensional deformable arteries. Computer Methods in
631 Applied Mechanics and Engineering. 2006;195:5685-706.
632 [29] Johnston BM, Johnston PR, Corney S, Kilpatrick D. Non-Newtonian blood flow in human right
633 coronary arteries: steady state simulations. J Biomech. 2004;37:709-20.
634 [30] Johnston BM, Johnston PR, Corney S, Kilpatrick D. Non-Newtonian blood flow in human right
635 coronary arteries: Transient simulations. J Biomech. 2006;39:1116-28.
636 [31] Chen MC, Lu P-C, Chen JS, Hwang NH. Computational hemodynamics of an implanted coronary
637 stent based on three-dimensional cine angiography reconstruction. ASAIO journal. 2005;51:313-20.
638 [32] Boutsianis E, Dave H, Frauenfelder T, Poulikakos D, Wildermuth S, Turina M, et al.
639 Computational simulation of intracoronary flow based on real coronary geometry. European journal
640 of Cardio-thoracic Surgery. 2004;26:248-56.
641 [33] LaDisa JF, Jr., Guler I, Olson LE, Hettrick DA, Kersten JR, Warltier DC, et al. Three-Dimensional
642 Computational Fluid Dynamics Modeling of Alterations in Coronary Wall Shear Stress Produced by
643 Stent Implantation. Ann Biomed Eng. 2003;31:972-80.
644 [34] LaDisa JF, jr., Olson LE, Hettrick DA, Warltier DC, Kersten JR, Pagel PS. Axial stent strut angle
645 influences wall shear stress after stent implantation: analysis using 3D computational fluid dynamics
646 models of stent foreshortening. Biomedical engineering online. 2005;4:59.
647 [35] Kaazempur-Mofrad MR, Wada S, Myers JG, Ethier CR. Mass transport and fluid flow in stenotic
648 arteries: Axisymmetric and asymmetric models. International Journal of Heat and Mass Transfer.
649 2005;48:4510-7.
650 [36] Chaichana T, Sun Z, Jewkes J. Haemodynamic analysis of the effect of different types of plaques
651 in the left coronary artery. Computerized Medical Imaging and Graphics. 2013;37:197-206.
652 [37] Olufsen MS. Structured tree outflow condition for blood flow in larger systemic arteries.
653 American journal of physiology-Heart and circulatory physiology. 1999;276:H257-H68.
654 [38] Myers JG, Moore JA, Ojha M, Johnston KW, Ethier CR. Factors Influencing Blood Flow Patterns in
655 the Human Right Coronary Artery. Ann Biomed Eng. 2001;29:109-20.
656 [39] Moore JA, Rutt BK, Karlik SJ, Yin K, Ethier CR. Computational blood flow modeling based on in
657 vivo measurements. Ann Biomed Eng. 1999;27:627-40.
658 [40] Perktold K, Hofer M, Rappitsch G, Loew M, Kuban BD, Friedman MH. Validated computation of
659 physiologic flow in a realistic coronary artery branch. Journal of Biomechanics. 1997;31:217-28.
660 [41] Olufsen MS, Nadim A. On deriving lumped models for blood flow and pressure in the systemic
661 arteries. Mathematical Biosciences and Engineering. 2004;1:61-80.
662 [42] Vignon-Clementel IE, Alberto Figueroa C, Jansen KE, Taylor CA. Outflow boundary conditions for
663 three-dimensional finite element modeling of blood flow and pressure in arteries. Computer
664 Methods in Applied Mechanics and Engineering. 2006;195:3776-96.
665 [43] Kim H, Vignon-Clementel I, Figueroa C, LaDisa J, Jansen K, Feinstein J, et al. On coupling a
666 lumped parameter heart model and a three-dimensional finite element aorta model. Ann Biomed
667 Eng. 2009;37:2153-69.

668 [44] Milišić V, Quarteroni A. Analysis of lumped parameter models for blood flow simulations and
669 their relation with 1D models. ESAIM: Mathematical Modelling and Numerical Analysis.
670 2004;38:613-32.
671 [45] Wellnhofer E, Osman J, Kertzscher U, Affeld K, Fleck E, Goubergrits L. Flow simulation studies in
672 coronary arteries—Impact of side-branches. Atherosclerosis. 2010;213:475-81.
673 [46] Bertolotti C, Deplano V. Three-dimensional numerical simulations of flow through a stenosed
674 coronary bypass. Journal of Biomechanics. 2000;33:1011-22.
675 [47] Frauenfelder T, Lotfey M, Boehm T, Wildermuth S. Computational fluid dynamics: hemodynamic
676 changes in abdominal aortic aneurysm after stent-graft implantation. Cardiovascular And
677 Interventional Radiology. 2006;29:613-23.
678 [48] Katritsis DG, Theodorakakos A, Pantos I, Gavaises M, Karcanias N, Efstathopoulos EP. Flow
679 Patterns at Stented Coronary Bifurcations: Computational Fluid Dynamics Analysis. Circulation:
680 Cardiovascular Interventions. 2012;5:530-9.
681 [49] Morris PD, Ryan D, Morton AC, Lycett R, Lawford PV, Hose DR, et al. Virtual Fractional Flow
682 Reserve From Coronary Angiography: Modeling the Significance of Coronary LesionsResults From the
683 VIRTU-1 (VIRTUal Fractional Flow Reserve From Coronary Angiography) Study. JACC: Cardiovascular
684 Interventions. 2013;6:149-57.
685 [50] Koo B-K, Erglis A, Doh J-H, Daniels DV, Jegere S, Kim H-S, et al. Diagnosis of Ischemia-Causing
686 Coronary Stenoses by Noninvasive Fractional Flow Reserve Computed From Coronary Computed
687 Tomographic AngiogramsResults From the Prospective Multicenter DISCOVER-FLOW (Diagnosis of
688 Ischemia-Causing Stenoses Obtained Via Noninvasive Fractional Flow Reserve) Study. Journal of the
689 American College of Cardiology. 2011;58:1989-97.
690 [51] Katritsis DG, Pantos I, Efstathopoulos EP, Tzanalaridou E, Korovesis S, Kourlaba G, et al. Three-
691 dimensional analysis of the left anterior descending coronary artery: comparison with conventional
692 coronary angiograms. Coronary Artery Disease. 2008;19:265-70.
693 [52] Katritsis DG, Pantos I, Korovesis S, Hadjipavlou M, Tzanalaridou E, Lockie T, et al. Three-
694 dimensional analysis of vulnerable segments in the left anterior descending artery. Coronary Artery
695 Disease. 2009.
696 [53] Katritsis DG, Efstathopoulos EP, Pantos J, Korovesis S, Kourlaba G, Kazantzidis S, et al. Anatomic
697 Characteristics of Culprit Sites in Acute Coronary Syndromes. Journal of Interventional Cardiology.
698 2008;21:140-50.
699 [54] Qiao A, Liu Y, Li S, Zhao H. Numerical Simulation of Physiological Blood Flow in 2-way Coronary
700 Artery Bypass Grafts. J Biol Phys. 2005;31:161-82.
701 [55] Mailhac A. JJB, J.T. Fallon, A. Fernandez-Ortiz, B. Meyer, J. H. Chesebro, V. Fuster and L.
702 Badimon. Effect of an eccentric severe stenosis on fibrin(ogen) deposition on severely damaged
703 vessel wall in arterial thrombosis. Relative contribution of fibrin(ogen) and platelets. Circulation.
704 1994;90:988-96.
705 [56] Kang M, Ji HS, Kim KC. In-vitro investigation of RBCs' flow characteristics and hemodynamic
706 feature through a microchannel with a micro-stenosis. Int J Biol and Biomed Eng. 2008;2:1-8.
707 [57] BETA-CAE SSA. META PostProcessor version 6.2.0. User's Guide. 2008.
708 [58] Ku DN. BLOOD FLOW IN ARTERIES. Annual Review of Fluid Mechanics. 1997;29:399-434.
709 [59] Levy RMBaNM. Cardiovascular Physiology St. Louis, USA: Mosby Inc.; 2001.
710 [60] Katritsis DG, Theodorakakos A, Pantos I, Andriotis A, Efstathopoulos EP, Siontis G, et al. Vortex
711 formation and recirculation zones in left anterior descending artery stenoses: computational fluid
712 dynamics analysis. Physics in Medicine and Biology. 2010;55:1395.
713 [61] Westerhof N, Boer C, Lamberts RR, Sipkema P. Cross-Talk Between Cardiac Muscle and Coronary
714 Vasculature2006.
715 [62] Soulis JV, Lampri OP, Fytanidis DK, Giannoglou GD. Relative residence time and oscillatory shear
716 index of non-Newtonian flow models in aorta. Biomedical Engineering, 2011 10th International
717 Workshop on: IEEE; 2011. p. 1-4.

718   [63] Shen F, Kastrup CJ, Liu Y, Ismagilov RF. Threshold Response of Initiation of Blood Coagulation by
719   Tissue Factor in Patterned Microfluidic Capillaries Is Controlled by Shear Rate. Arteriosclerosis,
720   Thrombosis, and Vascular Biology. 2008;28:2035-41.
721   [64] Doriot P-A, Dorsaz P-A, Dorsaz L, De Benedetti E, Chatelain P, Delafontaine P. In-vivo
722   measurements of wall shear stress in human coronary arteries. Coronary Artery Disease.
723   2000;11:495-502.
724   [65] Frauenfelder T, Boutsianis E, Schertler T, Husmann L, Leschka S, Poulikakos D, et al. In-vivo flow
725   simulation in coronary arteries based on computed tomography datasets: feasibility and initial
726   results. European radiology. 2007;17:1291-300.
727   [66] Banerjee RK, Back LH, Back MR, Cho YI. Physiological Flow Simulation in Residual Human
728   Stenoses After Coronary Angioplasty. Journal of biomechanical engineering. 2000;122:310-20.
729   [67] Pivkin IV, Richardson PD, Karniadakis G. Blood flow velocity effects and role of activation delay
730   time on growth and form of platelet thrombi. PNAS. 2006;103:17164-9.
731   [68] Miyazaki H, Yamaguchi T. Formation and destruction of primary thrombi under the influence of
732   blood flow and von Willebrand factor analyzed by a discrete element method. Biorheology.
733   2003;40:265-72.
734   [69] Cunningham KS, Gotlieb AI. The role of shear stress in the pathogenesis of atherosclerosis. Lab
735   Invest. 2005;85:9-23.
736   [70] Katritsis DG, Pantos J, Efstathopoulos E. Hemodynamic factors and atheromatic plaque rupture
737   in the coronary arteries: from vulnerable plaque to vulnerable coronary segment. Coronary Artery
738   Disease. 2007;18:229-37.
739   [71] Li ZY, Taviani V, Tang T, Sadat U, Young V, Patterson A, et al. The mechanical triggers of plaque
740   rupture: shear stress vs pressure gradient. Br J Radiol. 2009;82 Spec No 1:S39-45.
741   [72] Holme PA, Ørvim U, Hamers MJAG, Solum NO, Brosstad FR, Barstad RM, et al. Shear-Induced
742   Platelet Activation and Platelet Microparticle Formation at Blood Flow Conditions as in Arteries With
743   a Severe Stenosis. Arteriosclerosis, Thrombosis, and Vascular Biology. 1997;17:646-53.
744   [73] Feldman CL, Ilegbusi OJ, Hu Z, Nesto R, Waxman S, Stone PH. Determination of in vivo velocity
745   and endothelial shear stress patterns with phasic flow in human coronary arteries: a methodology to
746   predict progression of coronary atherosclerosis. American heart journal. 2002;143:931-9.
747   [74] Wurzinger LJ, Blasberg P, Schmid-Schonbein H. Towards a concept of thrombosis in accelerated
748   flow: rheology, fluid dynamics, and biochemistry. Biorheology. 1985;22:437-50.
749   [75] Papadopoulos KP, Gavaises M, Atkin C. A simplified mathematical model for thrombin
750   generation. Medical Engineering & Physics. 2013.
751   [76] Papadopoulos KP. Flow effect on thrombus formation in stenosed coronary arteries- A
752   computational study. London: City University London; 2015.
753   [77] Andriotis A, Zifan A, Gavaises M, Liatsis P, Pantos I, Theodorakakos A, et al. A new method of
754   three-dimensional coronary artery reconstruction from X-ray angiography: validation against a
755   virtual phantom and multislice computed tomography. Catheter Cardiovasc Interv. 2008;71:28-43.
756   [78] Kim KH, Doh JH, Koo BK, Min JK, Erglis A, Yang HM, et al. A novel noninvasive technology for
757   treatment planning using virtual coronary stenting and computed tomography-derived computed
758   fractional flow reserve. JACC Cardiovasc Interv. 2014;7:72-8.
759   [79] Min JK, Leipsic J, Pencina MJ, Berman DS, Koo BK, van Mieghem C, et al. Diagnostic accuracy of
760   fractional flow reserve from anatomic CT angiography. JAMA. 2012;308:1237-45.
761
762

763

9. Tables and Figures

stenosis	MI1			MI2			STA		
(%)	inflow	prox	dist	inflow	prox	dist	inflow	prox	dist
0	31.11	9.51	21.66	31.11	9.51	21.66	31.11	14.78	16.39
20	31.00	9.46	21.54	31.00	9.46	21.54	31.00	14.70	16.30
35	30.91	10.69	20.22	30.94	9.45	21.49	30.95	14.65	16.30
50	30.78	9.70	21.08	30.78	9.53	21.25	30.81	15.00	15.81
70	27.87	9.81	18.07	29.54	9.87	19.67	28.40	18.95	14.73
90	17.22	9.88	7.40	15.83	9.40	6.49	19.23	14.72	4.72

Table 1:

The effect of stenosis of flow rates. Calculated flow-rates in ml/min for the models with stenosis for the inlet, the outlets proximal to the peak of the stenotic lesion (prox) and the outlets distal the peak of the stenotic lesion (dist). The flowrates are expressed as a fraction of the respectively flow rates of the healthy model. All the groups follow similar pattern with the stenosis having important impact on the flow-rates only for high degree of stenosis ($\geq$ 70%).

772

stenosis	TAWSS								
	surface average			area with TAWSS>3Pa			area with TAWSS<0.15Pa		
	STA	MI1	MI2	STA	MI1	MI2	STA	MI1	MI2
0%	0.697			0.000			0.222		
20%	0.719	0.727	0.728	0.00	0.07	6.75	0.000	0.092	0.656
35%	0.750	0.747	0.765	0.00	0.49	0.88	0.139	2.010	1.072
50%	0.795	0.822	0.824	25.08	31.25	32.08	0.204	0.650	1.289
70%	0.994	1.113	1.012	25.53	36.73	36.01	0.442	0.044	0.364

Table 2

Average values of TAWSS for the whole geometry and surface of the geometry with TAWSS>3 and TAWSS<0.15 (area in mm^2). Coloured figures indicate the cases where the specific value is more than 25% (orange) or more than 50% (red) than the lowest (green) value among the models with same degree of stenosis

stenosis	OSI surface average(x1000)			OSI area with OSI>0.3			RRT surface average			RRT area with RRT>5		
	STA	MI1	MI2	STA	MI1	MI2	STA	MI1	MI2	STA	MI1	MI2
0%	7.62			0.00			1.57			1.41		
20%	5.49	5.41	5.63	0.00	0.00	0.05	1.54	1.51	1.52	1.26	1.06	2.15
35%	5.58	6.42	5.91	0.00	0.00	0.55	1.55	1.55	1.54	1.33	6.35	3.10
50%	8.23	10.39	11.02	4.59	6.77	9.78	1.72	1.70	1.78	12.58	18.30	19.88
70%	13.67	20.32	18.81	8.09	16.36	16.40	1.86	1.89	1.82	16.42	23.36	27.29

Table 3

Average values of OSI and RRT for the whole model and surface of the geometry
with OSI>0.3 and RRT>15 (area in mm^2). Coloured figures indicate that the specific
value is more than 25% (orange) or more than 50% (red) than the lowest (green)
value among the models with same degree of stenosis

Calculated Quantity	Minimum/maximum value	Maximum area/ threshold	Value for healthy model
Low WSS	<0.15 Pa	0.5mm^2	0.222 mm^2
High WSS	>3Pa	5mm^2	0 mm^2
OSI	>0.25	5mm^2	0.09 mm^2
RRT	>15 Pa^{-1}	2mm^2	1.41mm^2
CAI	n/a	1.2×10^{-5}m $\times$ s	0.95×10^{-5}m $\times$ s

786 **Table 4**

787 Proposed indices and threshold values for assessing the complication risk of
788 stenosed coronary arteries. For the surface related quantities the risk is estimated
789 based on the magnitude of the surface where the calculated quantity exceeds a
790 specific value, while for the CAI the calculations are explained in detail within the
791 text.

792

793

	Index	Low TAWSS	High TAWSS	OSI	RRT	CAI
	Model					
20%	**STA**	-(0.0)	-(0.0)	-(0.0)	-(0.63)	-(0)
	MI1	-(0.18)	-(0.014)	-(0.0)	-(0.53)	-(0.59)
	MI2	**+(1.3)**	**+(1.4)**	-(0.010)	**+(1.1)**	**+(1.6)**
35%	**STA**	-(0.28)	-(0.00011)	-(0.0)	(-0.66)	-(0.72)
	MI1	**+(4.2)**	-(0.098)	-(0.0)	**+(3.2)**	**+(2.8)**
	MI2	**+(2.1)**	-(0.18)	-(0.11)	**+(1.55)**	**+(2.0)**
50%	**STA**	-(0.41)	**+(5.0)**	-(0.91)	**+(6.3)**	-(0.88)
	MI1	**+(1.3)**	**+(6.3)**	**+(1.36)**	**+(9.1)**	**+(1.6)**
	MI2	**+(2.6)**	**+(6.4)**	**+(3.0)**	**+(9.9)**	**+(2.2)**
70%	**STA**	-(0.88)	**+(5.11)**	**+(1.7)**	**+(8.2)**	**+(1.3)**
	MI1	-(0.088)	**+(7.2)**	**+(3.27)**	**+(12)**	-(0.41)
	MI2	-(0.73)	**+(7.2)**	**+(3.28)**	**+(14)**	**+(1.2)**

794 **Table 5**

795 Indices of risk for the different models. The + and – signs indicate whether the value

796 of the index is above the suggested threshold while the number in the parenthesis is

797 the fraction of the threshold to the specific value. In the cases where the value

798 exceeds the suggested limit the digits are red.

799   **Figure 1**

800   **Geometrical models:** The averaged normal LAD model, the locations of the stenotic

801   regions for the different groups of geometries and the resulting models. The location

802   of maximum stenosis is at the middle of each lesion. The starting and ending

803   position of each lesion refer to the length of the centreline of the main branch of the

804   model, measured from the inlet.
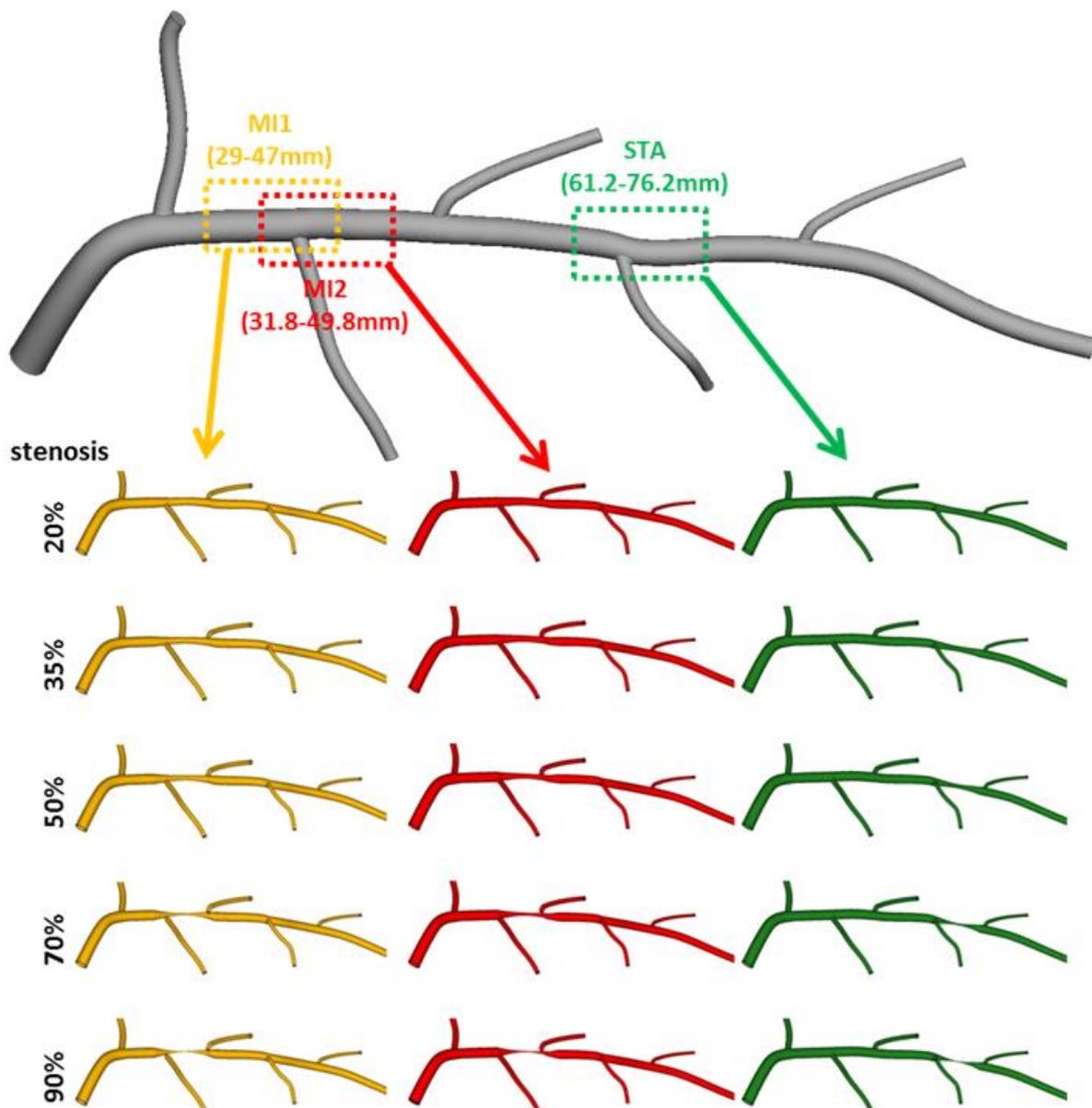
805

806

807   **Figure 2**

808   **Inlet waveforms:** Average velocity waveform for the inlet of the healthy coronary

809   model and pressure waveform that was used as inlet boundary condition for the

810   stenosed models.
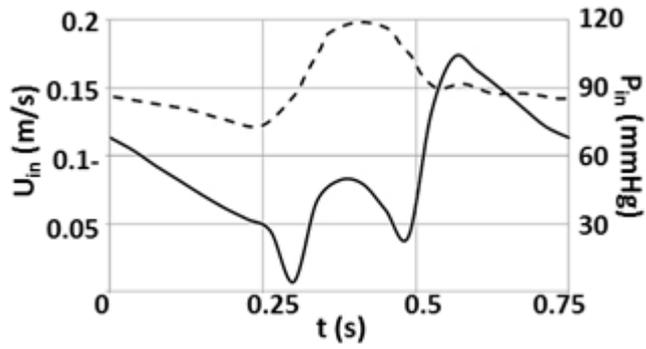
811

812

813 **Figure 3**

814 The steps used for the application of the time dependent resistance on the outlets. In

815 the equations ρ is the density of the fluid and A_i the surface of the boundary. The plot

816 is showing the process for the m-th iteration of the n-th time step, starting from the

817 values of the last iteration of the previous time step (n-1).

818
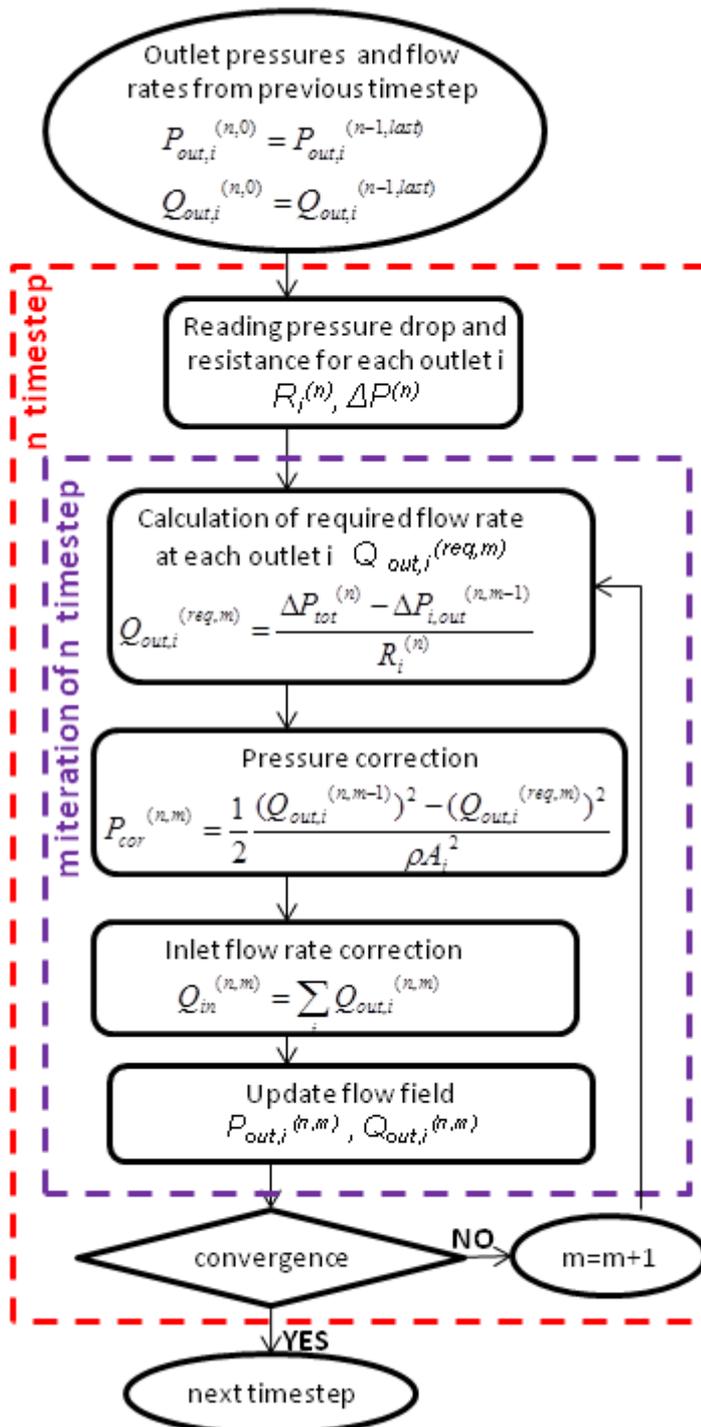
Figure 4

820 **Average velocity profiles:** Time averaged velocity profiles downstream the stenotic

821 lesion and the profiles of the non stenosed geometry in the same locations. Note that

822 a small difference in the location of the stenosis (<3mm, less than 20% of the total

823 length of the whole lesion) as it is between MI1 and MI2, changes significantly the

824 location of the areas with inversed average flow velocity.
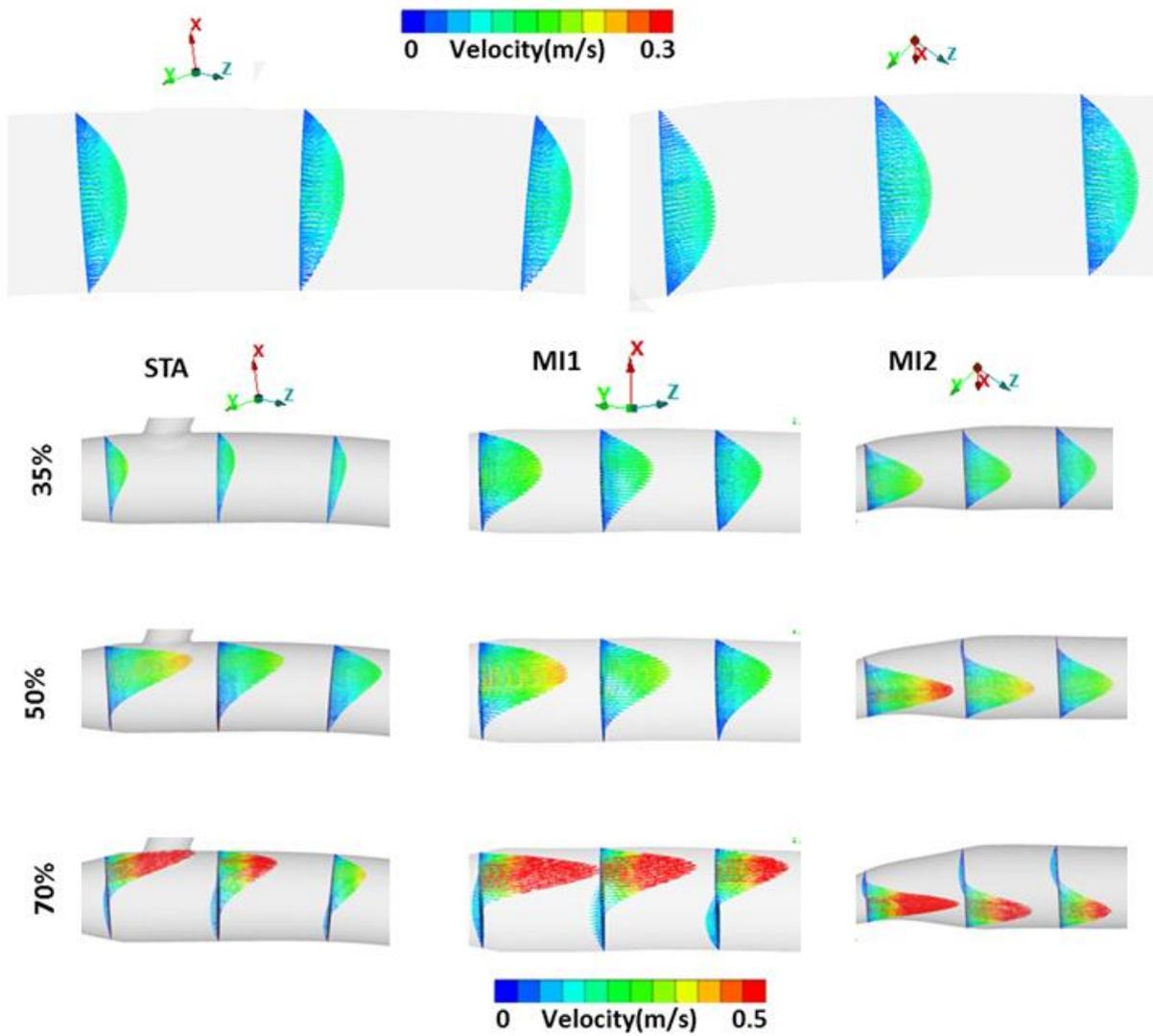
825

826

827 **Figure 5**

828 **Recirculation zones:** Recirculation zones downstream the stenotic lesion. Magenta

829 streamlines indicate that part of the flow from the vortex area ends up in the side

830 branch mainly in MI1 cases. Vortex stream-wise length is considerably larger for MI1

831 and MI2 models. All snapshots correspond to the same instance of the pulse.
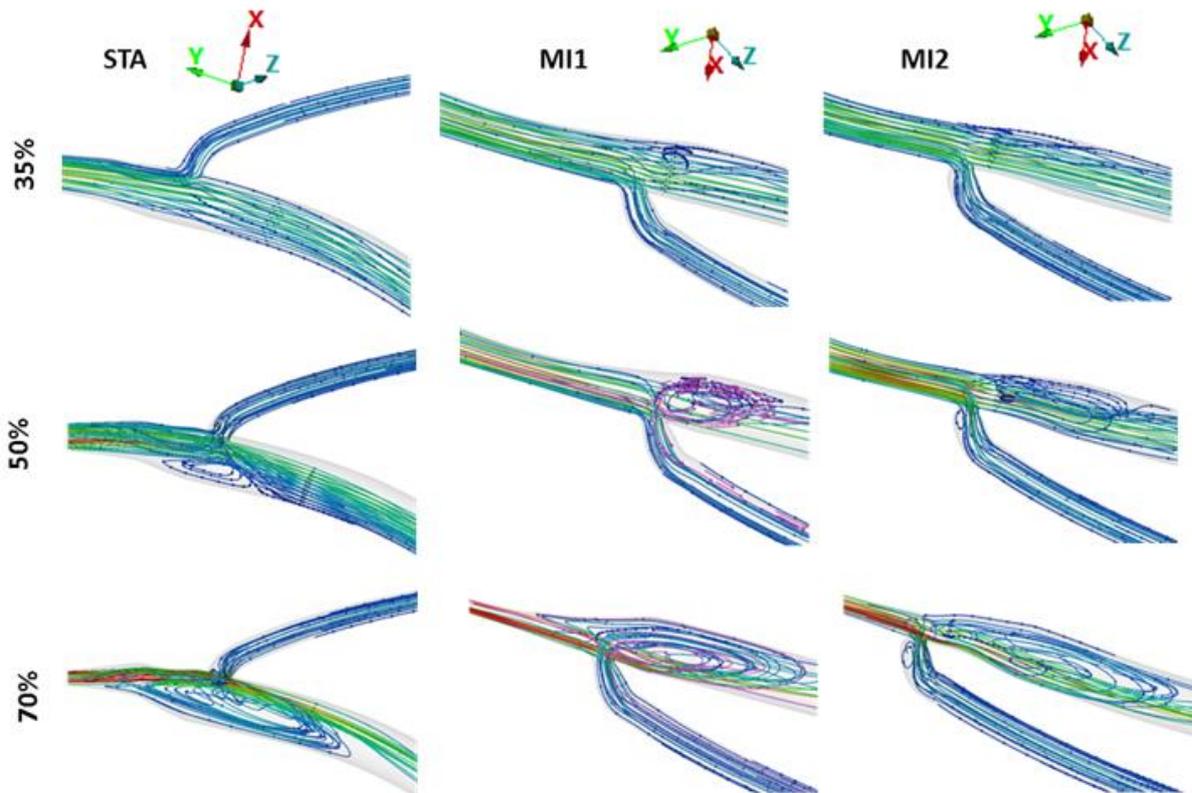
832

833 **Figure 6**

834 **Distribution of TAWSS-Areas with low TAWSS:** Contours of TAWSS for the

835 different models. The black areas are the segments of the vessel wall with

836 TAWSS<0.15Pa; note that in M1 and MI2 cases with 35% and 50% stenosis these

837 areas are significantly larger. Also, in MI1 and MI2 models with 70% there are areas

838 with high TAWSS (>5Pa) after the stenotic lesion while in all other model this is

839 restricted near the point of maximum stenosis.
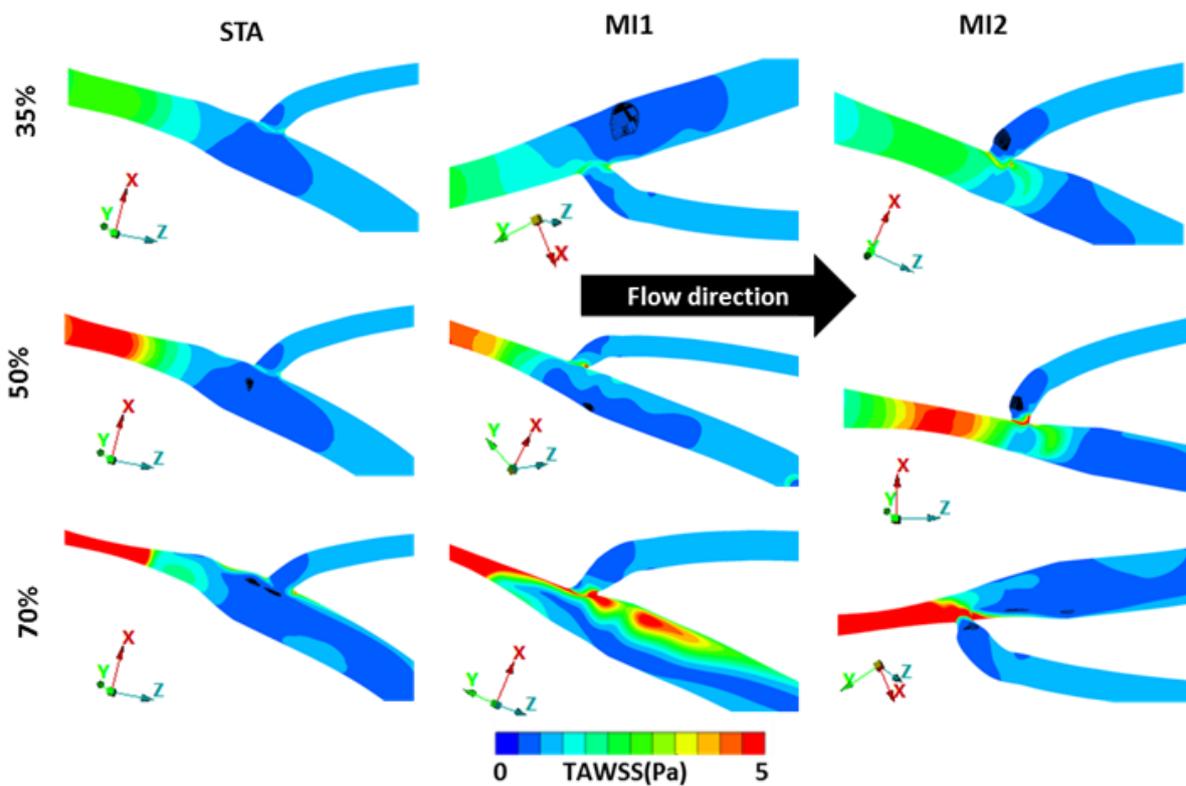

840

841 **Figure 7**

842 **Distribution of RRT:** Contours of RRT. For great degrees of stenosis the areas with

843 high RRT values are moved downstream. MI1 and MI2 have larger areas with high

844 RRT, and in MI2 models there is also an area with high RRT in the side branch after

845 the stenosis.
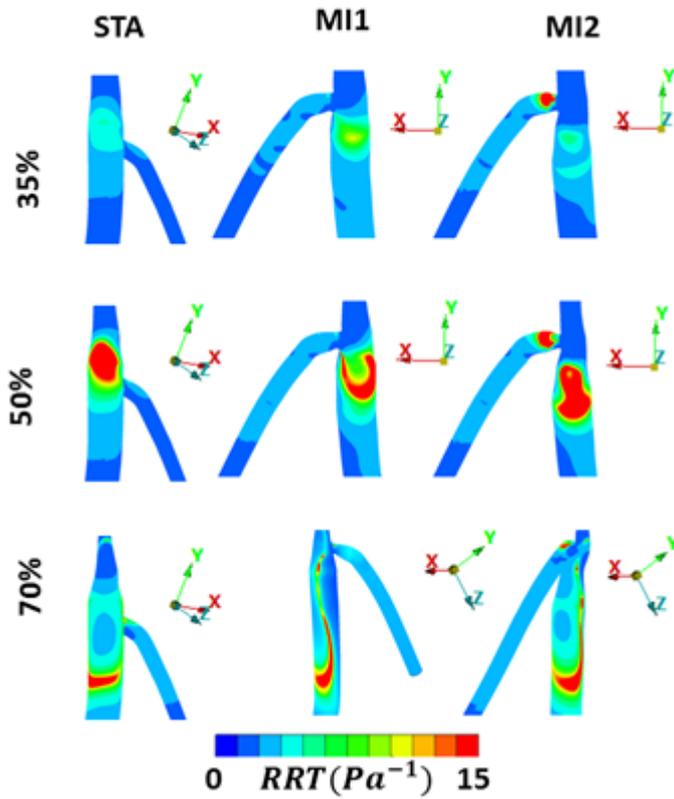
846

847   **Figure 8**

848   **Area with high OSI and RRT for different models:** Area of the vessel wall with

849   OSI and RRT above certain values. The areas with high RRT and OSI are

850   definitively higher for MI2 and MI1 geometries compared to STA for the same degree

851   of stenosis, but the change of these values is also strongly affected by the degree of

852   stenosis.
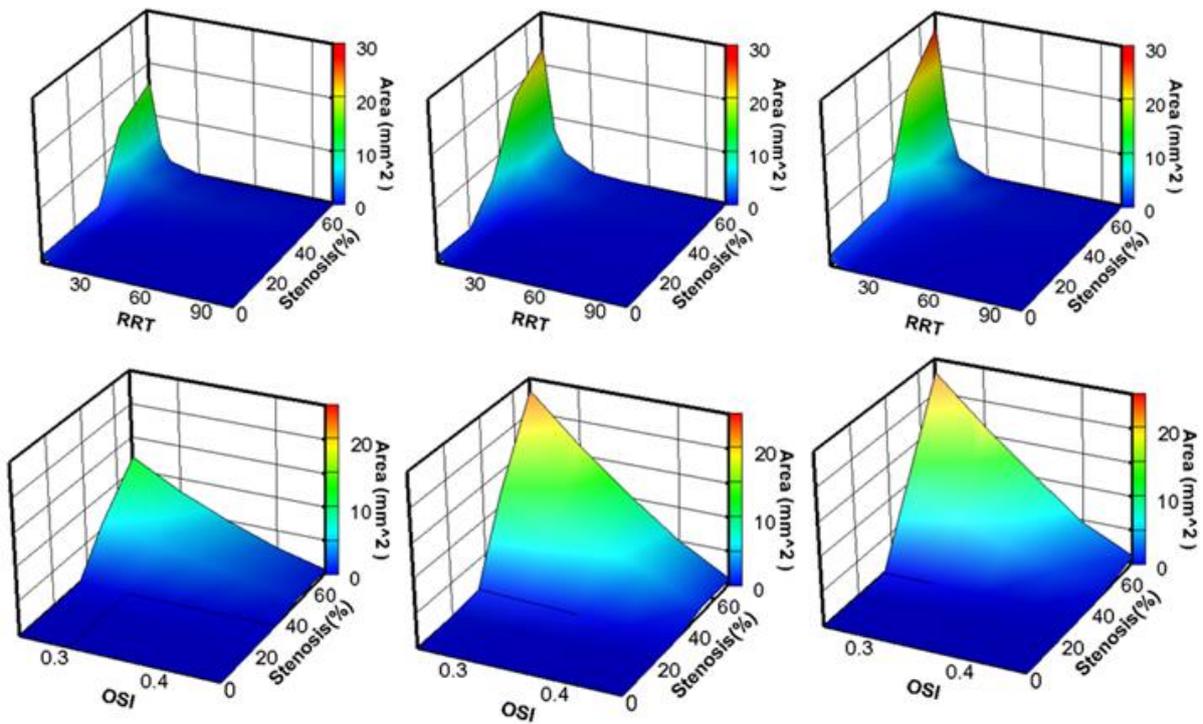
853

854

855 **Figure 9**

856 **Coagulation activation index for all models:** Variation of CAI for STA (×) MI1 (■)

857 and MI2 (●) geometries compared to the proposed threshold value (dashed line - -)

858 for different degrees of stenosis. For the geometries of MI1 and MI2 with

859 intermediate stenosis the value of CAI is clearly above the threshold line.

860